The Astrophysical Journal, 833:16 (9pp), 2016 December 10 doi:10.3847/0004-637X/833/1/16

PORTRAIT OF A DARK HORSE: A PHOTOMETRIC AND SPECTROSCOPIC STUDY OF THE ULTRA-FAINT MILKY WAY SATELLITE PEGASUS III*

Dongwon Kim[1], Helmut Jerjen[1], Marla Geha[2], Anirudh Chiti[3], Antonino P. Milone[1], Gary Da Costa[1], Dougal Mackey[1], Anna Frebel[3], and Blair Conn[1]
[1] Research School of Astronomy and Astrophysics, Australian National University, Canberra, ACT 2611, Australia; dongwon.kim@anu.edu.au
[2] Astronomy Department, Yale University, P.O. Box 208101, New Haven, CT 06510, USA
[3] Department of Physics and Kavli Institute for Astrophysics and Space Research, Massachusetts Institute of Technology, Cambridge, MA 02139, USA
Received 2016 August 15; revised 2016 October 4; accepted 2016 October 5; published 2016 December 2

ABSTRACT

Pegasus III (Peg III) is one of the few known ultra-faint stellar systems in the outer halo of the Milky Way. We present the results from a follow-up campaign with Magellan/IMACS and Keck/DEIMOS. Deep stellar photometry down to $r_0 \approx 25$ mag at 50% completeness level has allowed accurate measurements of its photometric and structural properties. The color–magnitude diagram of Peg III confirms that the stellar system is well described by an old ($\gtrsim$12 Gyr) and metal-poor ([Fe/H] $\lesssim -2.0$ dex) stellar population at a heliocentric distance of 215 ± 12 kpc. The revised half-light radius $r_h = 53 \pm 14$ pc, ellipticity $\epsilon = 0.38^{+0.22}_{-0.38}$, and total luminosity $M_V = -3.4 \pm 0.4$ are in good agreement with the values quoted in our previous paper. We further report on the spectroscopic identification of seven, possibly eight, member stars of Peg III. The Ca II triplet lines of the brightest member stars indicate that Peg III contains stars with metallicity as low as [Fe/H] $= -2.55 \pm 0.15$ dex. Peg III has a systemic velocity of -222.9 ± 2.6 km s^{-1} and a velocity dispersion of $5.4^{+3.0}_{-2.5}$ km s^{-1}. The inferred dynamical mass within the half-light radius is $1.4^{+3.0}_{-1.1} \times 10^6 M_\odot$ and the mass-to-light ratio $M/L_V = 1470^{+5660}_{-1240}$ $M_\odot/L_\odot$, providing further evidence that Peg III is a dwarf galaxy satellite. We find that Peg III and another distant dwarf satellite Pisces II lie relatively close to each other ($\Delta d_{\rm spatial} = 43 \pm 19$ kpc) and share similar radial velocities in the Galactic standard-of-rest frame ($\Delta v_{\rm GSR} = 12.3 \pm 3.7$ km s^{-1}). This suggests that they may share a common origin.

Key words: Local Group – planets and satellites: individual (Pegasus III, Pisces II)

1. INTRODUCTION

The census of satellite galaxies and star clusters associated with the Milky Way (MW) has been continuously updated for the last decade. Following the success of the Sloan Digital Sky Survey (SDSS; York et al. 2000), which revealed the presence of "ultra-faint" ($M_V > -5$) MW satellites (e.g., Willman et al. 2005; Belokurov et al. 2006; Zucker et al. 2006; Irwin et al. 2007; Koposov et al. 2007; Walsh et al. 2007; Balbinot et al. 2013; Kim & Jerjen 2015a), recent wide-field photometric surveys have been instrumental in finding many more such systems in the MW halo, and probing to increasingly faint levels (e.g., Bechtol et al. 2015; Drlica-Wagner et al. 2015; Kim et al. 2015b, 2016; Kim & Jerjen 2015b; Koposov et al. 2015a; Laevens et al. 2015a, 2015b; Martin et al. 2015; Luque et al. 2016; Torrealba et al. 2016a, 2016b). A growing number of the newly discovered MW satellites are filling the gap between the classical dwarf galaxies and globular clusters in the size–luminosity plane, meaning that it is increasingly difficult to classify these systems using only these two parameters (Willman & Strader 2012). Instead, the approach of determining their kinematics or chemistry still remains valid as a main diagnostic for distinguishing the two types of stellar systems (e.g., see discussions in Belokurov et al. 2014; Laevens et al. 2014; Kirby et al. 2015c; Voggel et al. 2016; Weisz et al. 2016). Spectroscopic follow-ups for the kinematic and chemical properties are rapidly catching up with the discoveries of the new satellites, but it is a technical challenge to study more than a handful of member stars in these systems due to their intrinsic low total luminosities and therefore lack of bright red giant branch (RGB) stars (Kirby et al. 2015a; Koposov et al. 2015b; Martin et al. 2015, 2016a, 2016b; Simon et al. 2015; Walker et al. 2015, 2016; Ji et al. 2016; Roederer et al. 2016).

Pegasus III (Peg III hereafter) is an MW satellite galaxy originally found in the SDSS Data Release 10 photometry (Ahn et al. 2014) by Kim et al. (2015a), who also provided detection confirmation at the $\sim 10\sigma$ level based on DECam photometry. The follow-up imaging with DECam further revealed the presence of six blue-horizontal-branch (BHB) candidate stars. Their apparent magnitudes implied that Peg III is located at a heliocentric distance of 205 ± 20 kpc in the outer region of the MW halo. From the relatively shallow DECam photometry, Peg III appeared to be elongated with a rather irregular stellar distribution, possibly indicative of tidal disturbance. Deeper imaging was thus required to confirm its true nature.

Peg III is a member of the small population of presently known MW satellites in the distance range 130 kpc $< d_{\rm GC} <$ 250 kpc. It is also located close to another distant satellite, Pisces II (Psc II hereafter, $d_\odot \sim 180$ kpc; Belokurov et al. 2010). These two satellites seem to form a physical pair with an angular separation of $8\overset{\circ}{.}5$ on the sky and a relatively small difference in the line-of-sight distance of $\sim$30 kpc. Other close pairs of MW satellites have been reported before—for example, Boötes I (Belokurov et al. 2006) and Boötes II (Walsh et al. 2007), Leo IV (Belokurov et al. 2007) and Leo V (Belokurov et al. 2008), or Horologium I (Bechtol et al. 2015; Koposov et al. 2015a) and Horologium II (Kim & Jerjen 2015b), leading to speculations about their companionship or common origin. The most notable pair is Leo IV–V,

* This paper includes data gathered with the 6.5 m Magellan Telescopes located at Las Campanas Observatory, Chile.

another pair of distant satellites ($d_{\odot} > 150$ kpc), for which the systemic line-of-sight velocities differ only by $\sim$40 km s^{-1} (Simon & Geha 2007; Belokurov et al. 2008), supporting the scenario that the pair might be gravitationally bound as a "tumbling pair" (de Jong et al. 2010). In this context, the discovery of another close pair of distant MW satellites naturally raises the question as to whether their systemic velocities are also similar to each other. To find an answer requires spectroscopic follow up to obtain their kinematic information.

We observed Peg III with Magellan/IMACS for deep photometry and Keck/DEIMOS for spectroscopy in order to firmly establish its luminosity and structural parameters, estimate its dynamic mass-to-light ratio, and investigate its possible association with Psc II.

2. PHOTOMETRY AND ASTROMETRY

We observed Peg III on 2015 July 22nd with the f/4 mode of the Inamori-Magellan Areal Camera & Spectrograph (IMACS) at the Magellan/Baade Telescope in the g and r bands. Magellan/IMACS has eight 2k $\times$ 4k CCDs with a total field of view of 15.′4 $\times$ 15.′4 and a pixel scale of 0.″2 pixel^{-1} (2 $\times$ 2 binning).

We obtained a series of 17 $\times$ 600s dithered exposures in g and 15 $\times$ 600s in r together with 20 bias frames, 10 dome flats in each filter taken before the science exposures, and 7 sky flats for each filter taken at the end of our observing night. During the observing run, the weather was clear and seeing ranged from 0.″8 to 1.″2. We produced the master bias and master flats using the zerocombine and flatcombine tasks in IRAF, and then carried out bias subtraction and flat fielding using the imarith task.

To find the astrometric solutions for the reduced science images, we used SCAMP (Bertin 2006) and the SDSS DR 10 photometry catalog.[4] We then combined the reduced images into our final image stacks using SWARP (Bertin et al. 2002).

We performed point-spread function (PSF) photometry on the final image stacks using SExtractor/PSFex (Bertin & Arnouts 1996; Bertin 2011). These software programs provide the SPREAD_MODEL parameter that allows morphological star/galaxy separation, for which we set a threshold |SPREAD_MODEL| $<$ 0.003 + SPREADERR_MODEL (see, e.g., Desai et al. 2012; Koposov et al. 2015a). This selection process was applied to the g-band image stack, which has a longer total integration time than the r-band image stack. After crossmatching the g and r catalogs using STILTS (Taylor 2005) with a 1″ tolerance, we converted the instrumental magnitudes of the matched catalog into the SDSS photometric system using unsaturated stars in common with our DECam photometry catalog for Peg III presented in Kim et al. (2015a), via bootstrap sampling with 500 iterations and 3σ clipping. Finally, we corrected the calibrated magnitudes for Galactic extinction based on the reddening map by Schlegel et al. (1998) and the correction coefficients from Schlafly & Finkbeiner (2011). In the studied field of view, the typical value of $E(B-V)$ is $\sim$0.124.

We note that the magnitudes of seven objects in the star catalog were replaced by average measurements from two best-seeing individual exposures as they fell onto the edges or corners of CCD chips in some individual exposures and suffered the extra-widening of the PSF relative to the typical full width half maximum (FWHM) in the process of image stacking. Such stacking-induced degrading of the PSF at CCD chip boundaries becomes more obvious when the individual exposures have a seeing difference as large as the pixel scale. We searched in our sample for stars brighter than $r_0 = 23$ mag that have been affected by the phenomenon, and found seven objects, including stars #1 and #8, in our spectroscopy sample (see Table 2). This effectively accounts to $\sim$2% of all objects in that magnitude range.[5] The number of such objects in the fainter magnitude range of $r_0 > 23$ mag where a typical FWHM is not well defined are not precisely determined. This phenomenon is, however, unlikely to significantly affect the rest of our analysis as the portion of the affected stars is small, the resulting magnitude difference is smaller than 0.1 mag, and the width of the photometric filtering mask used in Section 4 is sufficiently wide to take the effect into account.

We also measured the completeness levels of our photometry as a function of color and magnitudes using artificial stars as described in Kim et al. (2016). At the color $(g-r)_0 = 0.40$, the 90% and 50% completeness levels correspond to $r_0 = 22.65$ and $r_0 = 24.92$, respectively.

3. SATELLITE DISTANCE AND STELLAR POPULATION

The distribution of stars in our IMACS photometry and corresponding color–magnitude diagram are presented in Figure 1, reaching $\sim$3 mag fainter than our previous DECam photometry at the same signal-to-noise ratio (S/N) levels. The stars within an elliptical radius of 2.′55, equivalent to 3 half-light radii, of the center of Peg III are highlighted with black large dots. The stars outside the 3 half-light radii but within a circular radius of 2.′55 are also highlighted with smaller black dots to take into account the large uncertainty of the ellipticity derived in Section 4. The large red and blue dots in Figure 1 represent kinematically confirmed member and non-member stars, respectively (see Section 5 for more details).

We constrain the heliocentric distance of Peg III using the luminosity of its HB and the fiducial HB track of a globular cluster. Since the absolute total luminosity of Peg III was estimated to be -4.1 ± 0.5 in our previous work, the mean metallicity of the system is expected to be as low as [Fe/H] ~ -2.5 according to the mass–metallicity relation by Kirby et al. (2013). We note that the recent metallicity measurements of the MW satellite dwarf galaxies in the same luminosity range as Peg III; for example, Psc II ($\langle$[Fe/H]$\rangle = -2.45 \pm 0.07$; Kirby et al. 2015c) and Reticulum II ($\langle$[Fe/H]$\rangle = -2.65 \pm 0.07$; Simon et al. 2015) are consistent with the mass–metallicity relation. Accordingly, we adopted the fiducial HB sequence of M15, one of the most metal-poor globular clusters ([Fe/H] $= -2.42$), from Bernard et al. (2014). We converted the fiducial into the SDSS photometric system with the help of transformation equations and coefficients provided by Tonry et al. (2012). We took

[4] http://www.sdss3.org/dr10/

[5] We found the stars affected by the degrading of PSF in the g or r band by crossmatching catalogs from the stacked image and best-seeing individual frames, and filtering the matched catalog with the following criteria:

- $\mathrm{fwhm}_{\mathrm{indi}} < \overline{\mathrm{fwhm}_{\mathrm{indi}}} + 3\sigma_{\mathrm{fwhm,indi}}$
- $\mathrm{fwhm}_{\mathrm{stack}} > \overline{\mathrm{fwhm}_{\mathrm{stack}}} + 3\sigma_{\mathrm{fwhm,stack}}$
- $|\mathrm{SPREAD\_MODEL}_{\mathrm{indi}}| < 0.003 + \mathrm{SPREADERR\_MODEL}_{\mathrm{indi}}$.

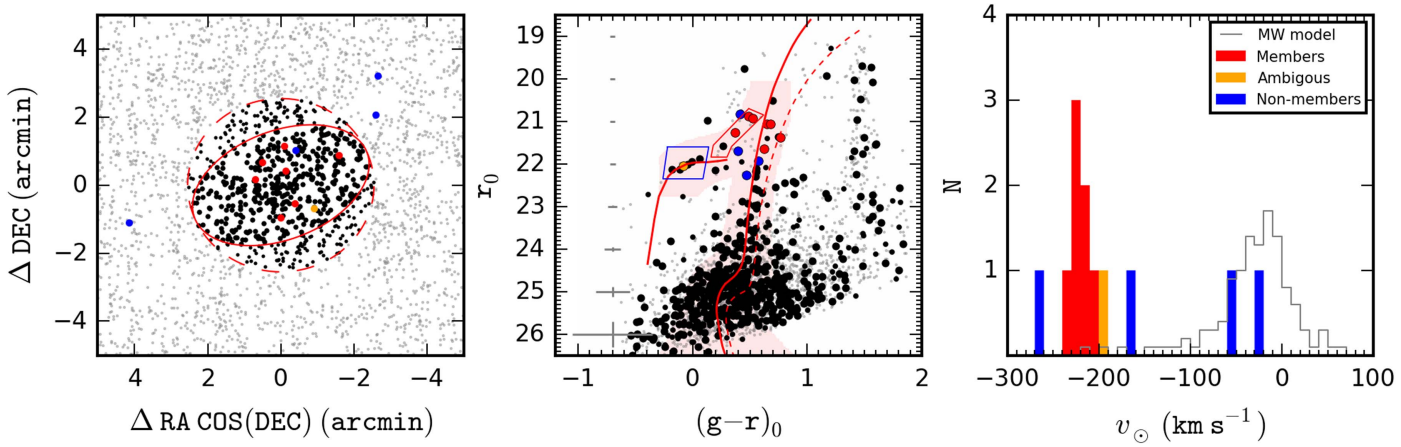

Figure 1. Left panel: distribution of all objects classified as stars in a 10.′0 × 10.′0 field centered on Peg III. Large black dots are the stars within an ellptical radius of 2.′55, equivalent to 3 half-light radii, of the center of Peg III (red ellpse) whereas the small dots are the stars outside the ellipse but within a circular-radial distance of 2.′55 (dashed circle). The red, blue, and orange large dots represent the 12 stars for which we obtained velocity measurements with Keck/DEIMOS, where red (blue) dots identify kinematic members (non-members). The small gray dots are the rest of the stars from our IMACS photometry. The large orange dot is a star whose membership is ambiguous. Middle panel: Magellan/IMACS CMD of the stars in the left panel. The symbols are the same as in the left panel. The two Dartmouth isochrones (Dotter et al. 2008) of age 13.5 Gyr, [Fe/H] = −2.5, and [α/Fe] = +0.4 (solid) and of age 12 Gyr, [Fe/H] = −1.1, and [α/Fe] = +0.2 (dashed) are overplotted at a distance of 215 kpc. The HB fiducial track has been derived from Bernard et al. (2014) by using the observed CMD of the globular cluster M15 ([Fe/H] = −2.42). The blue and red polygons highlight the HB and AGB/RHB candidate stars of Peg III, respectively. Right panel: radial velocity distribution of the 12 stars observed with Keck/DEIMOS. The colors are the same as in the left/middle panels. The solid line illustrates the predicted distribution of MW stars from the Besancon model (Robin et al. 2003), within a radius of 5.′0, normalized to the number of observed stars.

literature values of $E(B-V) = 0.11$ and $(m-M)_0 = 15.25$ (Kraft & Ivans 2003) to obtain the reddening-corrected fiducial HB sequence. We then expressed this fiducial HB sequence as a function of color $(g-r)_0$ by means of a fifth order polynomial regression, fit this function to the six BHB candidate stars in the blue polygon in the middle panel of Figure 1 with the least-squares method, and derived a distance modulus of $(m-M)_0 = 21.66 \pm 0.12$. For the uncertainty in the final estimate of the distance modulus, we combined in quadrature the uncertainties associated with our calibration to our DECam photometry (<0.01 mag), the adopted distance modulus of M15 (∼0.1 mag; Kraft & Ivans 2003), our fiducial HB sequence fit (0.03 mag, determined by jackknife resampling), and galactic reddening in the r band (<0.01 mag). In addition, we took into account the systematic uncertainty associated with the metallicity–luminosity relation, for which our estimate is ∼0.05 mag.

In the middle panel, a Dartmouth isochrone (Dotter et al. 2008) for age 13.5 Gyr, [Fe/H] = −2.5, and [α/Fe] = +0.4 (solid curve); an isochrone from the same set but for age 12 Gyr, [Fe/H] = −1.1, [α/Fe] = +0.2 (dashed curve); and the M15 fiducial HB sequence are plotted on the CMD at a distance modulus of $(m-M)_0 = 21.66$ or a heliocentric distance of 215 kpc. The three kinematic member stars in the red polygon appear systematically brighter than the BHB and bluer than the RGB. An excess of such stars relative to the RGB has been noticed in the CMD of the Hercules dwarf galaxy (e.g., Figure 2 in Sand et al. 2009) and the majority of them has been identified as its asymptotic giant branch (AGB) or red horizontal branch (RHB) population by photometric and spectroscopic studies (e.g., Adén et al. 2009; Fabrizio et al. 2014). Most likely the three Peg III member stars in the red polygon are AGB/RHB stars, too. Three of the other four kinematic members of Peg III are consistent with the RGB while the last one, star #2, is almost 0.1 mag redder. That color difference cannot be explained by photometric uncertainties alone. There are different factors that can cause a color spread in the RGB, including dispersions in metallicity and carbon abundances. The metallicity of stars in MW satellite dwarf galaxies with similar total luminosities to Peg III ranges largely from [Fe/H] = −3.5 up to [Fe/H] = −1.0 dex (e.g., Ursa Major II; Vargas et al. 2013). The red star #2 of Peg III can indeed be fitted with an isochrone for a higher metallicity of [Fe/H] = −1.1 (dashed curve in the middle panel) at the same distance modulus. Carbon stars ([Ca/Fe] ≫ +1.0) in dwarf galaxies also tend to be redder than carbon-normal RGB stars due to the Bond–Neff effect (Bond & Neff 1969), as shown for instance in Figure 7 of Kirby et al. (2015b). The possibility of a metallicity and carbon spread among the Peg III stars can be tested once the information on the chemical abundances of the individual stars becomes available. The low signal-to-noise of our spectra does not permit a detailed analysis for the chemical abundances of the individual targets.

We present a background-subtracted Hess diagram in Figure 2, which allows us to qualitatively assess the stellar population of Peg III by means of model isochrone fitting for different properties. The Hess diagram was constructed based on the CMD of all stars within the radial distance of 2.′55 and subtracting a control CMD of all stars in an equal area outside 4.′0. We overplot Dartmouth isochrones with different ages (8,10,12,13.5 Gyr) and metallicity [F/H] values (−2.5, −2.0, −1.5 dex). The [α/Fe] values for the isochrones are determined based on the [Fe/H]–[α/Fe] relation from Vargas et al. (2013). The distance modulus is fixed at 21.66 mag. The most notable difference among the isochrone fits is found in the main-sequence turnoff region, where the isochrones for metal-poor ([Fe/H] $\lesssim -2.0$) and old ($\gtrsim$12 Gyr) stellar populations appear to be most consistent. This suggests that Peg III shares similar properties, i.e., low metallicities and old ages, of stellar populations with previously known ultra-faint MW satellite dwarf galaxies (e.g., Brown et al. 2014 and references therein).

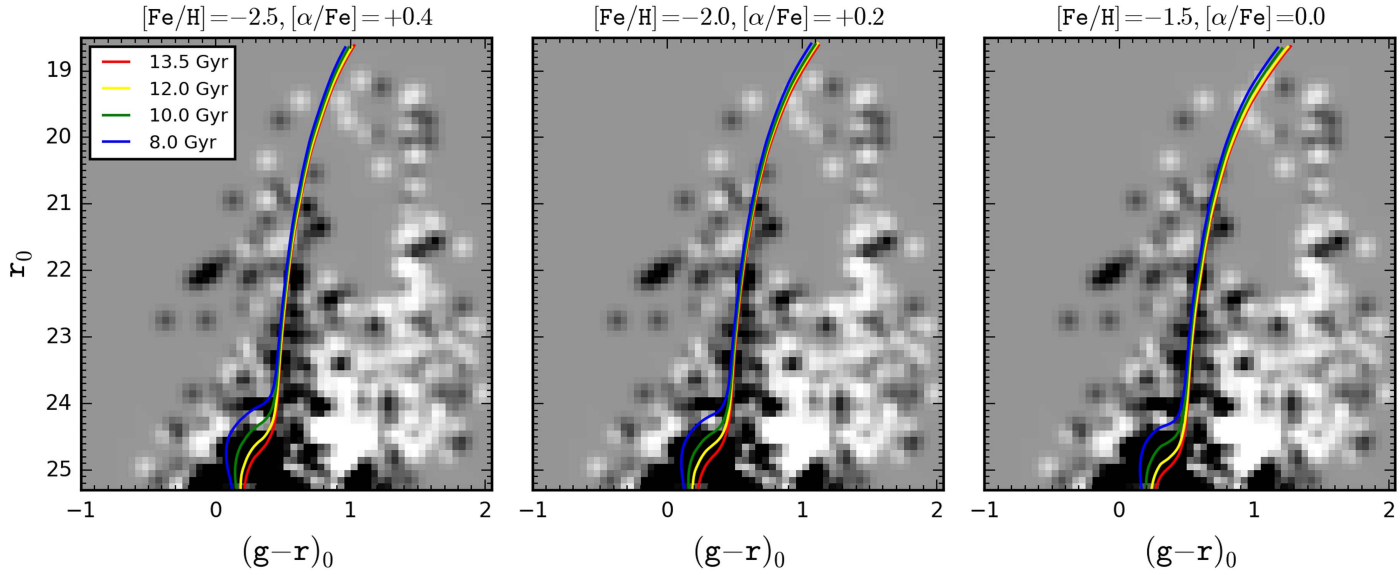

Figure 2. Background-subtracted Hess diagrams of Peg III within 2′.55 (dashed circle in the left panel of Figure 1). Overplotted are Dartmouth isochrones at a distance modulus of 21.66 mag for different ages, metallicities, and α abundances.

4. STRUCTURAL PROPERTIES AND ABSOLUTE LUMINOSITY

Figure 3 shows the convolved contour map of the star density centered on Peg III made of stars that passed a photometric filtering mask constructed from the Dartmouth isochrone for age 13.5 Gyr, [Fe/H] = −2.5, and [α/Fe] = +0.4 and the M15 HB fiducial line, as illustrated with a light-red shadow in Figure 1. The width of the mask gradually increases in the faint regime to take into account photometric uncertainties. The shape of the outer isodensity lines still remains irregular in the deep imaging data as previously seen in our DECam data (Kim et al. 2015a), which lends support to the scenario that the observed irregularity reflects the true structure, rather than being a consequence of the limited depth of the previous photometry. Given such a small population of stars in the system, however, assessing the observed irregularity is always subject to small number statistics (see, e.g., Martin et al. 2008; Walsh et al. 2008; Sand et al. 2010; Muñoz et al. 2012).

The central coordinates and structural parameters of Peg III were derived using the Maximum Likelihood (ML) routine as described in Kim et al. (2016) based on Martin et al. (2008) using our IMACS photometry catalog and the photometric filtering mask. The upper panels of Figure 4 show marginalized PDFs for key structural parameters. In this analysis, Peg III remains elliptical with $\epsilon = 0.38^{+0.22}_{-0.38}$ at a position angle of $\theta = 114^{+19}_{-17}$, but its half-light radius ($r_h = 53 \pm 14$ pc) appears ∼32% smaller than the previous estimate ($r_h = 78^{+30}_{-24}$ pc; Kim et al. 2015a). Nevertheless the two values are consistent at the 1σ level. The radial density profile with the best-fit exponential model based on the resulting values is presented in the lower panel of Figure 4. We further estimated the absolute luminosity of Peg III using the Dartmouth luminosity function (LF) for age 13.5 Gyr, [Fe/H] = −2.5, and [α/Fe] = +0.4 with the mass function by Chabrier (2001) as follows. We first normalized the theoretical LF and multiplied with the photometric completeness function derived in Section 2. We note that the Dartmouth isochrone accounts for RGB and MS stars but not AGB/HB sequences. We then integrated the scaled LF in the magnitude range of $r_0 > 22.0$ mag to calculate the probability density for the number of detected RGB/MS stars fainter than $r_0 = 22$ mag in our IMACS photometry. Accordingly, we repeated the ML routine using the previous filtering mask but excluding the AGB/HB sequences and the RGB sequence brighter than $r_0 = 22.0$ mag to estimate the number of RGB/MS stars fainter than $r_0 = 22.0$ mag that belong to the overdensity N with Equation (5) in Martin et al. (2008). The ratio of the star count N to the probability density allowed us to scale the normalized LF to the observed level. Integrating the upscaled LF estimates the integrated total luminosity of RGB/

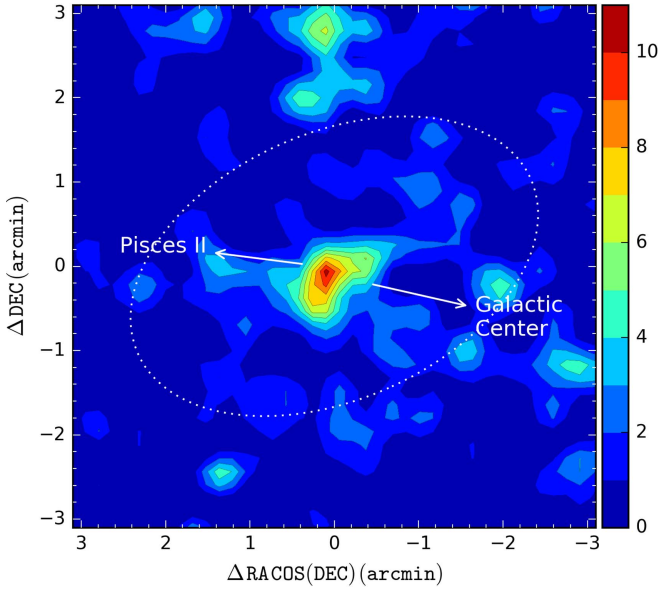

Figure 3. Convolved density contour map of Peg III candidate stars that pass the photometric filter illustrated in the middle panel of Figure 1. The density map was binned with a pixel size of 10″.0 and smoothed with a Gaussian kernel with FWHM of 23″.6. The contours mark the levels of star density in units of the standard deviation above the background (median value). The white dotted ellipse represents 3 half-light radii of the center of Peg III. The left and right arrows point to the nearby outer halo satellite Psc II and the Galactic Center, respectively.

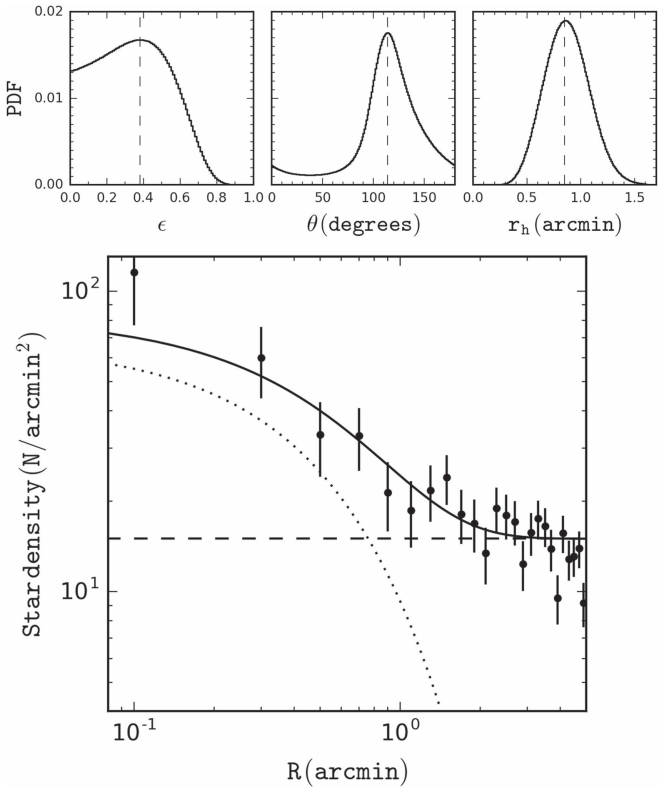

Figure 4. Upper panels: marginalized probability distrubtion functions (PDFs) of the structural parameters of Peg III. Lower panel: radial stellar density profile of Peg III. R is the elliptical radius. Overplotted are the best exponential model based on the parameters in Table 1 (dotted line), the contribution of foreground stars (dashed line), and the combined fit (solid line). The error bars were derived from Poisson statistics.

MS stars in Peg III as $M_r = -3.2^{+0.3}_{-0.4}$ or $M_V = -3.0^{+0.3}_{-0.4}$ by luminosity-weighted mean color $V - r = 0.17$ mag for the model LF. Finally, we calculated the flux of AGB/HB candidate stars in the red and blue polygons presented in the middle panel of Figure 1 using the transformation equation by Jordi et al. (2006) to convert their g and r magnitudes into V magnitudes. Their contribution increased the total luminosity in the V band by 0.4 mag and the uncertainty by 0.1 mag for the upper (fainter) limit and by less than 0.1 mag for the lower (brighter) limit. Therefore, we adopted $M_V = -3.4 \pm 0.4$ as our final estimate for the total luminosity of Peg III.

All the new estimates for the parameters are consistent with their previous estimates at the 1–σ level. The new values suggest that Peg III is somewhat smaller and fainter than previously estimated (Kim et al. 2015a). All resulting values presented in this and the next sections are summarized in Table 1.

5. SPECTROSCOPY

The data were taken with the Keck II 10 m telescope and the DEIMOS spectrograph (Faber et al. 2003). One multislit mask was observed in Peg III on the night of 2015 July 17. We selected 30 targets based on their color–magnitude distribution and distances from the center of the system using the DECam photometry from Kim et al. (2015a). We assigned priorities to potential RGB, AGB, and HB stars selected to follow the best-fitting isochrone to the CMD of Peg III in the DECam data. We used the 1200 line mm^{-1} grating that covers a wavelength range 6400–9100 Å at the spectral resolution 1.37 Å (FWHM, equivalent to 47 $km\,s^{-1}$ at the Ca II triplet). Slitlets were 0.″7 wide. The total exposure time was 2.5 hr.

Table 1
Properties of Peg III

Parameter	Value	Unit
α_{J2000}	22 24 24.48	h m s
δ_{J2000}	+05 24 18.0	° ′ ″
l	69.8452	deg
b	−41.8293	deg
$(m-M)_0$	21.66 ± 0.12	mag
$d_\odot$	215 ± 12	kpc
r_h	0.85 ± 0.22	′
	53 ± 14	pc
ϵ	$0.38^{+0.22}_{-0.38}$	⋯
θ	114^{+19}_{-17}	deg
M_V	−3.4 ± 0.4	mag
L_V	1960 ± 720	$L_\odot$
$\langle v_\odot \rangle$	−222.9 ± 2.6	$km\,s^{-1}$
v_{GSR}	−67.6	$km\,s^{-1}$
σ_v	$5.4^{+3.0}_{-2.5}$	$km\,s^{-1}$
$M_{1/2}$	$1.4^{+3.0}_{-1.1}$	$10^6\,M_\odot$
M/L_V	1470^{+5660}_{-1240}	$M_\odot/L_\odot$

We reduced the data using a modified version of the DEIMOS spec2d software pipeline(Cooper et al. 2012; Newman et al. 2013). We refer the reader to Simon & Geha (2007) for a more detailed description of the radial velocity measurement method. We measured the spectra of 12 out of the 30 targets, and their median S/N per pixel ranged from 1.4 to 7.0.

The membership of the sample stars was determined based on radial velocity, position in the CMD, and distance from the center of the dwarf galaxy. We identify seven secure members shown in red in Figure 1. An eighth member (shown in Figure 1 in orange) is 30 $km\,s^{-1}$ away from the systemic velocity, but also has very large velocity errors. This star has the colors of a horizontal branch member star and may be a RR Lyrae star. We do not include this star in the calculations below.

The velocities for all the observed Peg III candidate members are presented in Table 2. We note that the color and magnitude of star #11 was taken from our previous DECam photometry as its PSF on the IMACS images in g band was considerably affected by a saturated object nearby.

6. METALLICITY

Given the low S/N of the spectra, we attempted to measure the spectra-averaged metallicity of the four brightest stars in our sample (#5, 6, 7, 10) using the Ca II triplet lines. The measured strength of the spectral lines for RGB stars can be calibrated to metallicity [Fe/H] based on the empirical relationship between the equivalent width and the luminosity offset from the HB of the system $V_0 - V_{0,HB}$ (e.g., Starkenburg et al. 2010; Da Costa 2016). The g_0 and r_0 magnitudes of the stars were converted into V_0 magnitudes using the Jordi et al. (2006) Pop II transformation equations. We calculated the $V_0 - V_{0,HB}$ of the member stars based on the distance moduli for Peg III and M15 in Section 3, for which we assumed the V_{HB} for M15 from Harris and $E(B-V) = 0.11$ from Kraft & Ivans (2003). After smoothing the observed spectra with a

Table 2
Keck/DEIMOS Target List

Object	R.A. (J2000) (deg)	Decl. (J2000) (deg)	$(g-r)_0$ (mag)	r_0 (mag)	$v_\odot$ (km s^{-1})	S/N (pixel^{-1})	Membership	Photometry
1	336.17139	5.38661	0.47	22.28	−165.26 ± 5.78	1.89	N	IMACS
2	336.10198	5.38908	0.77	21.39	−220.57 ± 4.71	5.04	Y	IMACS
3	336.08657	5.39344	−0.08	22.05	−193.35 ± 22.92	1.43	?	IMACS
4	336.09530	5.39583	0.37	21.27	−234.68 ± 3.84	4.32	Y	IMACS
5	336.11372	5.40772	0.49	20.88	−218.51 ± 3.64	7.00	Y	IMACS
6	336.09952	5.41176	0.65	21.07	−226.16 ± 5.04	5.73	Y	IMACS
7	336.11021	5.41590	0.53	20.94	−229.45 ± 5.29	6.56	Y	IMACS
8	336.07514	5.41965	0.63	21.65	−208.45 ± 6.66	4.10	Y	IMACS
9	336.09502	5.42197	0.58	21.94	−50.69 ± 6.94	2.72	N	IMACS
10	336.10019	5.42418	0.68	21.07	−218.26 ± 3.56	6.37	Y	IMACS
11	336.05841	5.43938	0.40	21.71	−260.11 ± 9.97	3.43	N	DECam
12	336.05740	5.45859	0.42	20.83	−25.71 ± 3.06	6.13	N	IMACS

5 pixel boxcar using the splot command in IRAF, we dealt with the spectra in two ways as follows. First, we add them all together in order to increase the S/N. The λ8542 Å and λ8662 Å Ca II line strengths were then measured using the procedure described in Da Costa (2016). The summed equivalent width $\sum W \approx 2.34$ Å and the average $V_0 - V_{0,\rm HB} \approx -0.63$ mag give a reduced equivalent width W' of 1.93 Å. Applying the metallicity calibration with Equation (2) in Da Costa (2016) yields [Fe/H] = −2.40 dex with an uncertainty of order 0.15 dex. We then added the spectra for stars #6 and #10, and for #5 and #7 together separately. Repeating the above measurement process on these two spectra, we obtained $\sum W \approx 2.72$ Å with average $V_0 - V_{0,\rm HB} \approx -0.74$ mag for stars #6 and #10, and $\sum W \approx 1.99$ Å with average $V_0 - V_{0,\rm HB} \approx -0.51$ mag for stars #5 and #7. These values transform into [Fe/H] = −2.24 dex and [Fe/H] = −2.55 dex with uncertanties of order 0.15 dex, respectively. At face value, this is inconsistent with the CMD where stars #6 and #10 appear ∼0.2 mag bluer than stars #5 and #7 and so should be more metal poor. Stars #6 and #10 are, however, possibly AGB stars to which the calibration process strictly may not apply. It must also be kept in mind that the S/N of the summed spectra, even after smoothing, remains low. Nevertheless, this result confirms that Peg III includes stars with metallicity as low as [Fe/H] = −2.55 ± 0.15 dex.

7. KINEMATICS

In order to characterize the kinematics of Peg III, we employed a simple "non-rotation" model based on the method of Drukier et al. (1998). This method assumes that the measured radial velocities have a Gaussian distribution with mean velocity $\langle v_\odot \rangle$ and dispersion σ_v. The likelihood of the ith measurement $v_i \pm \delta_i$ is then given by

$$L_i(v_i|\langle v_\odot \rangle, \sigma_v) = G(v_i|\langle v_\odot \rangle, \sqrt{\sigma_v^2 + \delta_i^2}), \quad (1)$$

where $G(x|\mu, \sigma)$ is a Gaussian function of x with the mean μ and the standard deviation σ. The likelihood for the available data set $D \equiv \{v_i\}_{i=1}^N$ is the product of the individual likelihoods:

$$L(D|\langle v_\odot \rangle, \sigma_v) = \prod_i L_i(v_i|\langle v_\odot \rangle, \sigma_v). \quad (2)$$

Applying Bayes' theorem leads to

$$P(\langle v_\odot \rangle, \sigma_v|D) \propto L(D|\langle v_\odot \rangle, \sigma_v) P(\langle v_\odot \rangle, \sigma_v), \quad (3)$$

where $P(\langle v_\odot \rangle, \sigma_v|D)$ is the the posterior probability and $P(\langle v_\odot \rangle, \sigma_v) \equiv P(\langle v_\odot \rangle) P(\sigma_v)$ is the prior. For the mean velocity, the appropriate prior is a uniform prior $P(\langle v_\odot \rangle) = C$, for which we have set a finite range between −200 and −245 km s^{-1} to make it normalizable. In the case of the velocity dispersion, the appropriate prior is the Jeffreys prior $P(\sigma_v) \propto \sigma_v^{-1}$ (see, e.g., Drukier et al. 1998, 2007; Koposov et al. 2015b; Torrealba et al. 2016b), which is "non-informative" for a scale parameter such as the dispersion σ_v (see Section VII of Jaynes 1968 for justification). In fact, the choice of the prior has minimal impact on the posterior probability once the data are sufficiently constraining with a large sample size and small measurement errors. Otherwise, a uniform prior leads to a biased estimate for a scale parameter (see, e.g., Section 3.8 of Gregory 2005; Eriksen et al. 2008). Since the Jeffreys prior $P(\sigma_v) \propto \sigma_v^{-1}$ is also an improper prior, it requires reasonable bounds to turn into a proper prior such that the likelihood distribution is not significantly truncated (see, e.g., Section 3.3 in Drukier et al. 2007). We have set a finite interval for the prior $\sigma_v \in (1, 30)$ km s^{-1}, where the lower bound is ∼1/5 of the typical error on our measurements. We note that the likelihood for $\sigma_v \in (0, 1)$ km s^{-1} is equivalent to only 0.5% of that for $\sigma_v \in (0, 30)$ km s^{-1}.

The upper panel of Figure 5 shows the resulting posterior probability distribution in two-dimensional (2D) space, which appears asymmetric, spreading out toward larger velocity dispersions, most likely due to the small sample size (see, e.g., Figure 2 in Walker et al. 2009). The lower panels show the corresponding marginalized PDFs (solid curves) and also the PDFs constructed with a uniform prior on the velocity dispersion for comparison (dotted curves). Noticeably, the uniform prior favors larger velocity dispersions and displaces the modal value by +1.2 km s^{-1}. When it comes to determining the typical values and related uncertainties of the parameters, two different methods are commonly used in the literature: (a) find the modal values of the marginalized PDFs and the values that correspond to 61% of the peak probability for the confidence interval (e.g., Martin et al. 2014) or (b) read the 16, 50, and 84 percentiles of the marginalized PDFs (e.g., Walker et al. 2015). The results from each method are: (a) $\langle v_\odot \rangle = -222.9 \pm 2.6$ km s^{-1} and $\sigma_v = 5.4^{+3.0}_{-2.5}$ km s^{-1} and (b) $\langle v_\odot \rangle = -222.8^{+3.0}_{-2.9}$ km s^{-1} and $\sigma_v = 6.2^{+3.7}_{-2.7}$ km s^{-1}. We note

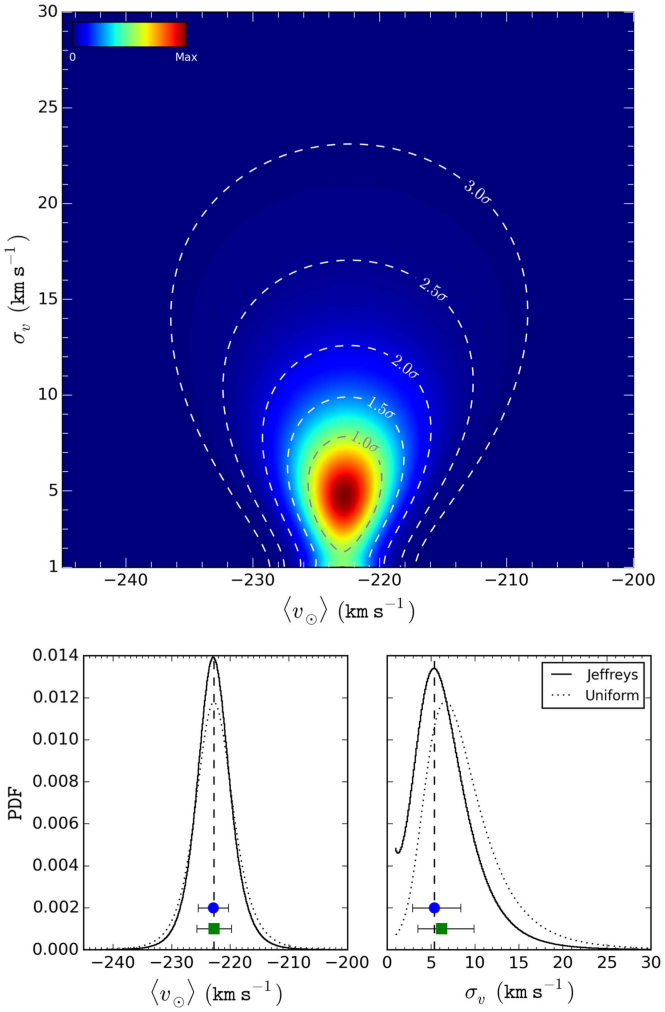

Figure 5. Upper panel: two-dimensional posterior probability distribution for the mean velocity and velocity dispersion of Peg III. Contours outline the 1σ–3σ confidence levels. (In two dimensions, Gaussian densities within 1σ, 2σ, and 3σ correspond to 39.3%, 86.5%, and 98.9%, respectively.) Lower panels: corresponding marginalized PDFs (solid curves). The PDFs for a uniform prior on the velocity dispersion are overplotted for comparison (dotted curves). All the PDFs are normalized such that each PDF covers an equal probability density underneath. The dashed lines correspond to the modal values of the marginalized posterior PDFs. The circle and square with error bars indicate the typical values and uncertainties determined by methods (a) and (b) in Section 7, respectively.

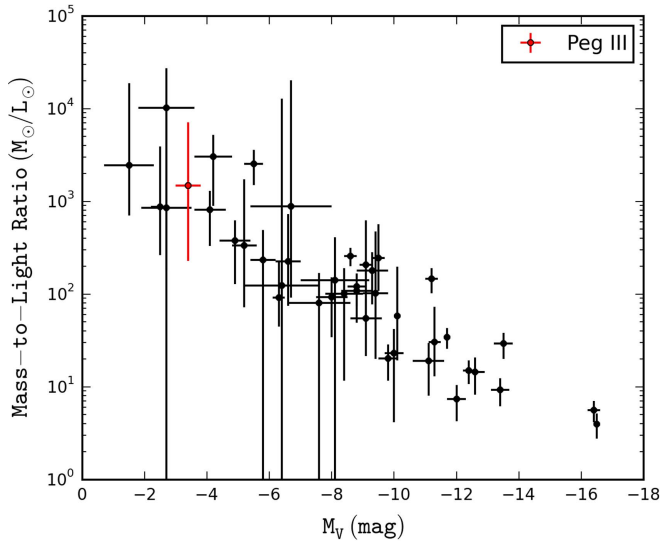

Figure 6. Mass-to-light ratio of Peg III (red) in comparison with other nearby galaxies within 1 Mpc. Mass-to-light ratios were calculated from the velocity dispersion, angular sizes (half-light radii), heliocentric distances, and absolute magnitudes collected by McConnachie (2012) for consistency with our estimate for Peg III. For the objects given "symmetric" uncertainties on the parameters, the error bars were determined based on the regular error propagation, and for the rest based on the upper and lower limits of the parameters.

that the inclusion of the ambiguous star #3 with $v_\odot = -193.35 \pm 22.92\,\mathrm{km\,s^{-1}}$ in our sample does not make a significant difference in the results as follows: (a) $\langle v_\odot \rangle = -222.5 \pm 2.6\,\mathrm{km\,s^{-1}}$ and $\sigma_v = 5.4^{+3.1}_{-2.4}\,\mathrm{km\,s^{-1}}$, and (b) $\langle v_\odot \rangle = -222.3^{+3.1}_{-2.9}\,\mathrm{km\,s^{-1}}$ and $\sigma_v = 6.3^{+3.8}_{-2.8}\,\mathrm{km\,s^{-1}}$. On the other hand, the exclusion of star #4 with $v_\odot = -234.68 \pm 3.84\,\mathrm{km\,s^{-1}}$ from our sample leads to an unresolved solution for the velocity dispersion, no matter which one of the above two priors is used. We noticed the same phenomenon in a test with the member stars for Psc II reported by Kirby et al. (2015c); removing the star ID10694 with $v_\odot = -232.0 \pm 1.6\,\mathrm{km\,s^{-1}}$ causes an unresolved solution. In an experiment with the kinematic members of Segue 1 reported by Simon et al. (2011), we found that such an unresolved solution occurs in ∼50% of the cases when 6 stars are randomly selected out of 32 stars having comparable measurement errors ($2 < \delta_v < 7\,\mathrm{km\,s^{-1}}$) and Bayesian membership probabilities larger than 90%. This variation is even larger than the 1–σ uncertainty of the velocity dispersion and the influence of binary stars in the sample (∼0.5 km s^{-1}; see Figure 6 in Simon et al. 2011). This result therefore suggests that the unresolved solutions are most likely a consequence of the small sample size. We will adopt the values and uncertainties obtained from method (a) as our final estimates in Table 1 and throughout the text. It is interesting to note that the measured systemic velocity for Peg III is very similar to that found for its neighboring satellite Psc II ($\langle v_\odot \rangle = -226.5 \pm 2.7\,\mathrm{km\,s^{-1}}$) independently measured by Kirby et al. (2015c).

Assuming dynamical equilibrium, the mass enclosed within the half-light radius of a stellar system can be accurately measured by the following equation as demonstrated by Wolf et al. (2010):

$$M_{1/2} \simeq \frac{4}{G}\,\sigma_v^2\,r_h\,M_\odot, \tag{4}$$

where σ_v is the line-of-sight velocity dispersion and r_h is the 2D projected half-light radius. According to this relation, the mass within the elliptical half-light radius of Peg III is estimated to be $M_{1/2} = 1.4^{+3.0}_{-1.1} \times 10^6\,M_\odot$. The absolute magnitude of Peg III we derived in Section 4 translates into a total luminosity of $1960 \pm 720\,L_\odot$, which corresponds to a mass-to-light ratio of $M/L_V = 1470^{+5660}_{-1240}\,M_\odot/L_\odot$. This value is consistent with the inverse correlation between luminosity and mass-to-light ratio for other nearby dwarf galaxies (see Figure 6).

8. DISCUSSION AND SUMMARY

We have obtained Magellan/IMACS photometry and Keck/DEIMOS spectroscopy for Peg III. The deep photometry confirms that Peg III is a faint ($M_V = -3.4 \pm 0.4$), elongated ($\epsilon = 0.38^{+0.22}_{-0.38}$), irregular, and distant ($d_\odot = 215 \pm 12$ kpc) stellar system. We measured radial velocities for individual

candidate member stars and identified seven, possibly eight, member stars in the system based on their radial velocities, where the member stars could be either red giants or AGB stars (red large dots in Figure 1). The stellar population of Peg III contains stars with metallicity as low as $[\mathrm{Fe/H}] = -2.55 \pm 0.15$ dex. The velocity dispersion of Peg III ($\sigma_v = 5.4^{+3.0}_{-2.5}\,\mathrm{km\,s^{-1}}$) significantly exceeds the value expected from its observed stellar mass alone ($<0.3\,\mathrm{km\,s^{-1}}$; see Table 5 in Pawlowski et al. 2015), which supports the picture that Peg III is a satellite dwarf galaxy rather than a star cluster.

Peg III and Psc II are approximately 43 kpc away from each other in three dimensions (3D) and their radial velocities in the Galactic standard-of-rest (GSR) frame differ only by $\sim$10 km s^{-1} ($v_{\mathrm{GSR}} = -67.6 \pm 2.6\,\mathrm{km\,s^{-1}}$ for Peg III and $v_{\mathrm{GSR}} = -79.9 \pm 2.7\,\mathrm{km\,s^{-1}}$ for Psc II). Given that only relatively few distant MW satellite galaxies are presently known, the close spatial proximity of Peg III and Psc II, and their very similar radial velocities suggest a possible association between them. We note that another companionship of two distant MW satellites has been previously identified, namely the Leo IV–Leo V pair. Despite the difference in their radial velocities in the GSR frame ($\Delta v_{\mathrm{GSR}} \sim 50\,\mathrm{km\,s^{-1}}$, Simon & Geha 2007; Belokurov et al. 2008), their close spatial proximity in 3D ($\Delta d_{\mathrm{spatial}} \sim 22$ kpc) has led to the hypothesis of a possible physical connection or common origin (e.g., de Jong et al. 2010). Such a companionship of two satellites, as Walker et al. (2009) suggested, may imply a rather circular orbit on which MW tides have a minimum effect. Assuming that the two satellites are currently a bound pair with an equal halo mass and follow a circular orbit on their average Galactocentric distance of $\sim$198 $\pm$ 10 kpc, we have estimated their total halo mass following the method of Evslin (2014). This method estimates the mass of the binary satellite system on the basis of the virial theorem using the difference in their line-of-sight velocities ($12.3 \pm 3.7\,\mathrm{km\,s^{-1}}$) and the separation between its constituents ($d_{\mathrm{spatial}} = 43 \pm 19$ kpc) in 3D space. The derived mass of a satellite halo is $2.3 \pm 1.7 \times 10^9\,M_\odot$, which yields a tidal radius of $r_t = 16 \pm 4$ kpc. The ratio of the separation to the tidal radius is $d_{\mathrm{spatial}}/r_t = 2.7 \pm 1.0$. At face value, the tidal radius is smaller than the separation, in which case the binding energy of the two satellites is too low to remain undisrupted in the MW tidal field. This result, however, does not entirely rule out the possibility of a physical pair as the tidal radius is comparable to the separation at the 1.7σ level. Information about their tangential velocities and dark-matter halo profiles, as well as more accurate measurements for other parameters, would provide more constraints on this result.

In both our DECam and IMACS photometry, Peg III appears irregular and elongated ($\epsilon = 0.38^{+0.22}_{-0.38}$), at the 1-$\sigma$ limit, compared to Psc II, which only has an upper limit for its measured ellipticity ($\epsilon < 0.28$; Sand et al. 2012) with an unconstrained position angle. In fact, a similarity is found with the Leo IV–V pair (see Table 7 in Sand et al. 2012), where Leo V features larger ellipticity ($\epsilon = 0.55 \pm 0.22$) with an unconstrained position angle and lower luminosity ($M_V = -4.4 \pm 0.4$) than Leo IV ($\epsilon < 0.23$, $M_V = -5.5 \pm 0.3$). We consider three possible scenarios for the origin of the ellipticity of Peg III. The first is that it is simply a result of its formation process. The second is that it results from tidal interaction with the MW. Under the assumption that the stars of Peg III are in dynamic equilibrium this seems unlikely, given (a) the large velocity dispersion implying a substantial mass, (b) the compact physical size, (c) the elongation misaligned with the direction toward the Galactic center, and (d) the likelihood that Peg III and Psc II are moving on similar circular or near circular orbits at large Galactocentric distances. On the other hand, if the large velocity dispersion of the Peg III stars reflects a non-equilibrium state or being inflated by unresolved binary stars rather than the presence of a large amount of dark matter, then the system might be a remnant of a dwarf galaxy tidally disrupted by the MW. This would require the orbit of Peg III to be significantly eccentric in order to reach the required smaller Galactocentric distances. In turn, this would make the spatial and velocity agreement with Psc II coincidental, which seems highly unlikely. The third alternative is that the ellipticity of Peg III results from a tidal interaction with Psc II. To test these different ideas will require *N*-body simulations or full 3D orbit information (i.e., the radial velocities and proper motions of the objects). Much deeper and wider imaging or higher resolution spectroscopy with new forthcoming telescopes such the *Wide-Field Infrared Survey Telescope* (*WFIRST*) and the Giant Magellan Telescope (GMT) may provide crucial keys to these questions.

The authors thank the anonymous referee for helpful suggestions that improved the clarity and quality of the paper. We also thank Holger Baumgardt, Mila Chadayammuri, Joshua Simon, John Norris, and David Yong for interesting discussions and valuable comments. HJ and BC acknowledge the support of the Australian Research Council through Discovery projects DP120100475 and DP150100862. A.C. and A.F. acknowledge support from NSF-CAREER grant AST-1255160. A.P.M. acknowledges support by the Australian Research Council through Discovery Early Career Researcher Award DE150101816. G.D.C. and A.D.M. are grateful for support from the Australian Research Council through Discovery Projects DP120101237 and DP150103294.

This research made use of Astropy, a community-developed core Python package for Astronomy (Astropy Collaboration et al. 2013), and Matplotlib library (Hunter 2007).

Some of the data presented herein were obtained at the W.M. Keck Observatory, which is operated as a scientific partnership among the California Institute of Technology, the University of California and the National Aeronautics and Space Administration. The Observatory was made possible by the generous financial support of the W.M. Keck Foundation. The authors wish to recognize and acknowledge the very significant cultural role and reverence that the summit of Mauna Kea has always had within the indigenous Hawaiian community. We are most fortunate to have the opportunity to conduct observations from this mountain.

REFERENCES

Adén, D., Feltzing, S., Koch, A., et al. 2009, A&A, 506, 1147
Ahn, C. P., Alexandroff, R., Allende Prieto, C., et al. 2014, ApJS, 211, 17
Astropy Collaboration, Robitaille, T. P., Tollerud, E. J., et al. 2013, A&A, 558, A33
Balbinot, E., Santiago, B. X., da Costa, L., et al. 2013, ApJ, 767, 101
Bechtol, K., Drlica-Wagner, A., Balbinot, E., et al. 2015, ApJ, 807, 50
Belokurov, V., Irwin, M. J., Koposov, S. E., et al. 2014, MNRAS, 441, 2124
Belokurov, V., Walker, M. G., Evans, N. W., et al. 2008, ApJL, 686, L83
Belokurov, V., Walker, M. G., Evans, N. W., et al. 2010, ApJL, 712, L103
Belokurov, V., Zucker, D. B., Evans, N. W., et al. 2006, ApJL, 647, L111
Belokurov, V., Zucker, D. B., Evans, N. W., et al. 2007, ApJ, 654, 897

Bernard, E. J., Ferguson, A. M. N., Schlafly, E. F., et al. 2014, MNRAS, 442, 2999
Bertin, E. 2006, in ASP Conf. Ser. 351, Astronomical Data Analysis Software and Systems XV, ed. C. Gabriel et al. (San Francisco, CA: ASP), 112
Bertin, E. 2011, in ASP Conf. Ser. 442, Astronomical Data Analysis Software and Systems XX, ed. I. N. Evans et al. (San Francisco, CA: ASP), 435
Bertin, E., & Arnouts, S. 1996, A&AS, 117, 393
Bertin, E., Mellier, Y., Radovich, M., et al. 2002, in ASP Conf. Ser. 281, Astronomical Data Analysis Software and Systems, ed. D. A. Bohlender, D. Durand, & T. H. Handley (San Francisco, CA: ASP), 228
Bond, H. E., & Neff, J. S. 1969, ApJ, 158, 1235
Brown, T. M., Tumlinson, J., Geha, M., et al. 2014, ApJ, 796, 91
Chabrier, G. 2001, ApJ, 554, 1274
Cooper, M. C., Newman, J. A., Davis, M., Finkbeiner, D. P., & Gerke, B. F. 2012, spec2d: DEEP2 DEIMOS Spectral Pipeline, Astrophysics Source Code Library, ascl:1203.003
Da Costa, G. S. 2016, MNRAS, 455, 199
de Jong, J. T. A., Martin, N. F., Rix, H.-W., et al. 2010, ApJ, 710, 1664
Desai, S., Armstrong, R., Mohr, J. J., et al. 2012, ApJ, 757, 83
Dotter, A., Chaboyer, B., Jevremović, D., et al. 2008, ApJS, 178, 89
Drlica-Wagner, A., Bechtol, K., Rykoff, E. S., et al. 2015, ApJ, 813, 109
Drukier, G. A., Cohn, H. N., Lugger, P. M., et al. 2007, AJ, 133, 1041
Drukier, G. A., Slavin, S. D., Cohn, H. N., et al. 1998, AJ, 115, 708
Eriksen, H. K., Jewell, J. B., Dickinson, C., et al. 2008, ApJ, 676, 10
Evslin, J. 2014, MNRAS, 440, 1225
Faber, S. M., Phillips, A. C., Kibrick, R. I., et al. 2003, Proc. SPIE, 4841, 1657
Fabrizio, M., Raimondo, G., Brocato, E., et al. 2014, A&A, 570, A61
Gregory, P. C. 2005, Bayesian Logical Data Analysis for the Physical Sciences (Cambridge: Cambridge Univ. Press)
Hunter, J. D. 2007, CSE, 9, 90
Irwin, M. J., Belokurov, V., Evans, N. W., et al. 2007, ApJL, 656, L13
Jaynes, E. T. 1968, IEEE Trans. Syst. Sci. Cybernetics, SSC-4, 227
Ji, A. P., Frebel, A., Chiti, A., & Simon, J. D. 2016, Natur, 531, 610
Jordi, K., Grebel, E. K., & Ammon, K. 2006, A&A, 460, 339
Kim, D., & Jerjen, H. 2015a, ApJ, 799, 73
Kim, D., & Jerjen, H. 2015b, ApJL, 808, L39
Kim, D., Jerjen, H., Mackey, D., Da Costa, G. S., & Milone, A. P. 2015a, ApJL, 804, L44
Kim, D., Jerjen, H., Mackey, D., Da Costa, G. S., & Milone, A. P. 2016, ApJ, 820, 119
Kim, D., Jerjen, H., Milone, A. P., Mackey, D., & Da Costa, G. S. 2015b, ApJ, 803, 63
Kirby, E. N., Cohen, J. G., Guhathakurta, P., et al. 2013, ApJ, 779, 102
Kirby, E. N., Cohen, J. G., Simon, J. D., & Guhathakurta, P. 2015a, ApJL, 814, L7
Kirby, E. N., Guo, M., Zhang, A. J., et al. 2015b, ApJ, 801, 125
Kirby, E. N., Simon, J. D., & Cohen, J. G. 2015c, ApJ, 810, 56
Koposov, S., de Jong, J. T. A., Belokurov, V., et al. 2007, ApJ, 669, 337
Koposov, S. E., Belokurov, V., Torrealba, G., & Evans, N. W. 2015a, ApJ, 805, 130
Koposov, S. E., Casey, A. R., Belokurov, V., et al. 2015b, ApJ, 811, 62
Kraft, R. P., & Ivans, I. I. 2003, PASP, 115, 143
Laevens, B. P. M., Martin, N. F., Bernard, E. J., et al. 2015a, ApJ, 813, 44
Laevens, B. P. M., Martin, N. F., Ibata, R. A., et al. 2015b, ApJL, 802, L18
Laevens, B. P. M., Martin, N. F., Sesar, B., et al. 2014, ApJL, 786, L3
Luque, E., Queiroz, A., Santiago, B., et al. 2016, MNRAS, 458, 603
Martin, N. F., Chambers, K. C., Collins, M. L. M., et al. 2014, ApJL, 793, L14
Martin, N. F., de Jong, J. T. A., & Rix, H.-W. 2008, ApJ, 684, 1075
Martin, N. F., Geha, M., Ibata, R. A., et al. 2016a, MNRAS, 458, L59
Martin, N. F., Ibata, R. A., Collins, M. L. M., et al. 2016b, ApJ, 818, 40
Martin, N. F., Nidever, D. L., Besla, G., et al. 2015, ApJL, 804, L5
McConnachie, A. W. 2012, AJ, 144, 4
Muñoz, R. R., Padmanabhan, N., & Geha, M. 2012, ApJ, 745, 127
Newman, J. A., Cooper, M. C., Davis, M., et al. 2013, ApJS, 208, 5
Pawlowski, M. S., McGaugh, S. S., & Jerjen, H. 2015, MNRAS, 453, 1047
Robin, A. C., Reylé, C., Derrière, S., & Picaud, S. 2003, A&A, 409, 523
Roederer, I. U., Mateo, M., Bailey, J. I., III, et al. 2016, AJ, 151, 82
Sand, D. J., Olszewski, E. W., Willman, B., et al. 2009, ApJ, 704, 898
Sand, D. J., Seth, A., Olszewski, E. W., et al. 2010, ApJ, 718, 530
Sand, D. J., Strader, J., Willman, B., et al. 2012, ApJ, 756, 79
Schlafly, E. F., & Finkbeiner, D. P. 2011, ApJ, 737, 103
Schlegel, D. J., Finkbeiner, D. P., & Davis, M. 1998, ApJ, 500, 525
Simon, J. D., Drlica-Wagner, A., Li, T. S., et al. 2015, ApJ, 808, 95
Simon, J. D., & Geha, M. 2007, ApJ, 670, 313
Simon, J. D., Geha, M., Minor, Q. E., et al. 2011, ApJ, 733, 46
Starkenburg, E., Hill, V., Tolstoy, E., et al. 2010, A&A, 513, A34
Taylor, M. B. 2005, in ASP Conf. Ser. 347, Astronomical Data Analysis Software and Systems, ed. P. Shopbell, M. Britton, & R. Ebert (San Francisco, CA: ASP), 29
Tonry, J. L., Stubbs, C. W., Lykke, K. R., et al. 2012, ApJ, 750, 99
Torrealba, G., Koposov, S. E., Belokurov, V., & Irwin, M. 2016a, MNRAS, 459, 2370
Torrealba, G., Koposov, S. E., Belokurov, V., et al. 2016b, MNRAS, 463, 712
Vargas, L. C., Geha, M., Kirby, E. N., & Simon, J. D. 2013, ApJ, 767, 134
Voggel, K., Hilker, M., Baumgardt, H., et al. 2016, MNRAS, 460, 3384
Walker, M. G., Belokurov, V., Evans, N. W., et al. 2009, ApJL, 694, L144
Walker, M. G., Mateo, M., Olszewski, E. W., et al. 2015, ApJ, 808, 108
Walker, M. G., Mateo, M., Olszewski, E. W., et al. 2016, ApJ, 819, 53
Walsh, S. M., Jerjen, H., & Willman, B. 2007, ApJL, 662, L83
Walsh, S. M., Willman, B., Sand, D., et al. 2008, ApJ, 688, 245
Weisz, D. R., Koposov, S. E., Dolphin, A. E., et al. 2016, ApJ, 822, 32
Willman, B., Blanton, M. R., West, A. A., et al. 2005, AJ, 129, 2692
Willman, B., & Strader, J. 2012, AJ, 144, 76
Wolf, J., Martinez, G. D., Bullock, J. S., et al. 2010, MNRAS, 406, 1220
York, D. G., Adelman, J., Anderson, J. E., Jr., et al. 2000, AJ, 120, 1579
Zucker, D. B., Belokurov, V., Evans, N. W., et al. 2006, ApJL, 643, L103